Ferromagnetic excited-state Mn^{2+} dimers in $Zn_{1-x}Mn_xSe$ quantum dots observed by time-resolved magnetophotoluminescence

Liam R. Bradshaw, Joseph W. May, Jillian L. Dempsey,* Xiaosong Li, and Daniel R. Gamelin†
Department of Chemistry, University of Washington, Seattle, Washington 98195-1700, USA
(Received 4 November 2013; revised manuscript received 24 February 2014; published 19 March 2014)

Colloidal Mn^{2+}-doped semiconductor nanocrystals are solution processable analogs of classic phosphor and diluted magnetic semiconductor materials with promising applications ranging from fluorescence microscopy to spintronic information processing. At doping levels of only a few cation mole percent, Mn^{2+} dimers form in appreciable concentration and cause shortened photoluminescence decay times and reduced luminescence circular polarization under applied magnetic fields. Here, we show that these differences allow the use of time-resolved magnetophotoluminescence measurements to investigate the magnetic properties of the luminescent dimer excited state in $Zn_{1-x}Mn_xSe$ nanocrystals. These measurements reveal that Mn^{2+}-Mn^{2+} dimers are coupled ferromagnetically in their luminescent excited state, in contrast with the antiferromagnetic coupling of their ground state. We find that Mn^{2+}-Mn^{2+} dimers also luminesce with much purer circular polarization than Mn^{2+} monomers under applied magnetic fields. These results are explained well by perturbation theory and density functional theory analyses of the microscopic orbital exchange interactions within the photoexcited Mn^{2+}-Mn^{2+} dimers. This discovery of photoswitchable dimer magnetism (from $S = 0$ to $S = 4$) with strong associated circularly polarized luminescence raises intriguing possibilities for optical spin manipulation in doped semiconductors.

DOI: 10.1103/PhysRevB.89.115312 PACS number(s): 78.20.Ls, 75.30.Hx, 75.50.Pp, 61.72.uj

I. INTRODUCTION

Mn^{2+}-doped semiconductors such as ZnSe or ZnS have been used as commercial phosphors for decades [1–3]. Doping Mn^{2+} into such semiconductors allows efficient sensitization of Mn^{2+}-centered $^4T_1 \rightarrow {}^6A_1$ *d-d* luminescence either through impact excitation of Mn^{2+} (electroluminescence) or via photoexcitation of the semiconductor followed by rapid energy localization at Mn^{2+} [2,4,5]. This localized *d-d* transition is formally spin forbidden and is consequently characterized by radiative decay times of milliseconds to microseconds (depending on the lattice anion). Because of the small absorption oscillator strengths of this and the other *d-d* transitions of Mn^{2+}, these doped semiconductors are also largely transparent at subbandgap energies. Colloidal nanocrystals (NCs) of the same compositions enable unique applications of these classic phosphor materials in solution-processed light-emitting devices [6–8], luminescent solar concentrators [9], or optical imaging experiments [10], and have furthermore revealed entirely new luminescence phenomena including intrinsic exciton/Mn^{2+} dual emission not yet realized in other forms of these phosphors [11]. Finally, the magnetism of Mn^{2+} also imparts exceptional magneto-optical and magnetoelectronic properties to the semiconductor, ultimately stemming from Mn^{2+}-carrier *sp-d* exchange interactions. These include giant Zeeman splittings of the semiconductor band edges and strong circularly polarized magnetoluminescence [12,13], motivating the development of photonic device structures that exploit the interplay between light and magnetism, such as spin-LEDs and spin-photonic transducers [14–17].

In their ground states, nearest-neighbor Mn^{2+}-Mn^{2+} dimers in II-VI and III-V semiconductors are antiferromagnetically coupled and hence magnetically silent ($|{}^6A_1,{}^6A_1\rangle$, $S = 0$), reducing the magnetization [18,19] and consequently the effective Mn^{2+} concentrations available for exchange interactions with free carriers [19]. Dimer formation is therefore generally detrimental to the desired magnetoelectronics or magneto-optical materials performance. Recently, a decrease in circular polarization of Mn^{2+} *d-d* magnetoluminescence was reported at elevated Mn^{2+} concentrations in doped semiconductor nanocrystals, from which it was hypothesized that circularly polarized photoluminescence (PL) arises primarily from isolated Mn^{2+} ions [12].

Essentially nothing is known about the excited-state magnetic properties of Mn^{2+}-Mn^{2+} dimers in II-VI semiconductors, even though the ground-state magnetic exchange coupling of such dimers has been studied extensively [20–33]. An understanding of dimer excited states is essential for evaluating how Mn^{2+} concentrations influence magnetoluminescence in this important class of materials, but the few relevant experimental results are either debated or inconclusive. In 1963, for example, McClure analyzed the energies of sharp absorption lines in the zero-phonon region of the monomer $^6A_1 \rightarrow {}^4E$ absorption of $Zn_{1-x}Mn_xS$ at high Mn^{2+} concentrations in terms of a dimer spin ladder ($|{}^6A_1,{}^6A_1\rangle \rightarrow |{}^4E,{}^6A_1\rangle$) and concluded a net ferromagnetic $|{}^4E,{}^6A_1\rangle$ excited-state exchange coupling [20], but Langer and Ibuki [26] later interpreted these sharp transitions as arising from phonon coupling, not magnetic exchange. Subsequent time-gated PL measurements showed that some of these lines originate from dimers (with faster PL decay), and the transitions were assigned assuming the same antiferromagnetic coupling in this excited state as in the $|{}^6A_1,{}^6A_1\rangle$ ground state [25].

Dimer formation can also affect intra-ion absorption and luminescence transition probabilities: The spin ladders generated by exchange coupling within transition-metal dimers introduce new formally spin-allowed pair transitions that have increased absorption oscillator strengths and radiative decay

*Present address: Department of Chemistry, University of North Carolina, Chapel Hill.
†Corresponding author: gamelin@chem.washington.edu

rate constants. This intensity-gaining mechanism has been investigated widely among exchange-coupled ion pairs and is referred to as the Tanabe mechanism [20,34–37].

Here, we describe the use of time-resolved (TR) magnetophotoluminescence spectroscopy to study Mn^{2+} spins in colloidal $Zn_{1-x}Mn_xSe$ nanocrystals. We show that this technique allows Mn^{2+}-Mn^{2+} dimers to be resolved from Mn^{2+} monomers, based on their shorter dimer luminescence decay times arising from the Tanabe mechanism. This experiment thus allows dimer excited-state magneto-optical properties to be analyzed separately from those of Mn^{2+} monomers. Time-resolved measurements show that the magnetic circularly polarized photoluminescence (MCPL) of Mn^{2+}-Mn^{2+} dimers saturates at lower magnetic fields than that of monomers, in a manner only consistent with a high-spin, i.e. ferromagnetically coupled ($S = 4$) dimer configuration. Additionally, these data reveal essentially complete (~100%) circular polarization in the dimer luminescence at magnetic saturation, in contrast with only ~40% polarization in Mn^{2+} monomer MCPL. This result is interpreted as resulting from a difference in the specific $\Delta m_s = \pm 1$ luminescence transitions available to the monomer and dimer excited states. Perturbation theory and density functional theory (DFT) calculations suggest that this dimer ferromagnetic excited-state exchange coupling originates from the dominance of a single orbital superexchange pathway in the luminescent $|^4T_1, {}^6A_1\rangle$ excited state. These results resolve the 50-year-old question of Mn^{2+}-Mn^{2+} dimer excited-state exchange coupling in doped semiconductors and point to new possibilities for optical spin manipulation in semiconductors of technological interest.

II. EXPERIMENTAL

A. Nanocrystal synthesis and characterization

$Zn_{1-x}Mn_xSe$ nanocrystals were synthesized by lyothermal degradation of the tetramer $[Zn_4(SePh)_{10}](Me_4N)_2$ in the presence of $MnCl_2$ and Se similar to previously published methods [38]. ZnS shells were grown on these cores by successive additions of zinc oleate and trioctylphosphine sulfide at 225 °C [39,40]. All $Zn_{1-x}Mn_xSe$ core NCs had diameters of d = 2.9–3.1 nm, and the $Zn_{1-x}Mn_xSe$/ZnS core/shell NCs had d = 3.7–4.0 nm. Mn^{2+} concentrations were determined by inductively coupled plasma atomic emission spectroscopy. All of the core/shell nanocrystals made following these procedures showed similar absorption and PL spectra to those reported here, and all had room-temperature PL quantum yields of ~40%. Additional synthesis and characterization details are provided in the Supplemental Material [41].

B. Spectroscopic measurements

Photoluminescence experiments were performed on partially evaporated films of NCs sandwiched between quartz plates. For magneto-optical measurements, samples were mounted in a superconducting magneto-optical cryostat with a variable-temperature sample compartment (Cryo-Industries SMC-1659 OVT or Oxford SM-2). Excitation was provided by a nitrogen-pumped dye laser operating at 360 nm, 20 Hz, with an 800-ps pulse width. The laser output was coupled into a multimode fiber and then refocused onto the sample at an incident angle of ~10° relative to the magnetic field axis. Photoluminescence was collected along the field axis and passed through a liquid crystal variable retardation plate (Meadowlark) set to $\lambda/4$ at the emission maximum followed by a linear polarizer to separate left and right circularly polarized components. The PL was then coupled into a fiber and passed to a monochromator equipped with LN_2 cooled charge-coupled device (CCD) and photomultiplier tube (PMT) detectors. Photoluminescence decay kinetics were measured using a multichannel scalar, averaging over several thousand laser pulses. Polarization ratios are reported in terms of left and right circularly polarized light intensities defined with the sign convention of Piepho and Schatz [13]. Because significant reductions in the MCPL ratios were noted for samples that depolarized or scattered light, all samples were checked for depolarization by measuring the circular dichroism signal from a chiral molecule placed before and after the sample prior to collection of MCPL data. All samples reported here showed depolarization of less than 10%. Nevertheless, we estimate uncertainties in absolute polarization ratios ($\Delta I/I$) of ~±0.07.

C. Computational methods

Quasispherical $Zn_{86-n}Mn_nSe_{86}$ quantum dots (QDs) were constructed using the bulk ZnSe zinc blende crystal structure with lattice parameter a = 5.6676 Å [42]. The effective diameters of the QDs are d ~ 2.2 nm, and in the absence of Mn^{2+} the QDs have C_{3v} symmetry. Pseudohydrogen atoms with nuclear charges of +1.5 and +0.5 were used to passivate uncompensated surface Zn^{2+} and Se^{2-} ions (dangling bonds) by formation of fully optimized Zn-H and Se-H bonds, according to the scheme described in recent literature [43–45], leading to a well-defined bandgap and stable QD geometry. Dopants were introduced by substituting either one or two Zn^{2+} ions near the center of the QD with Mn^{2+} to form a monomer or a bridged Mn^{2+}-Se^{2-}-Mn^{2+} dimer, respectively.

Density functional theory calculations were performed with the development version of the Gaussian program [46]. Full geometry optimizations of the doped QDs were performed in the ground and excited states for both the antiferromagnetic (AFM) and ferromagnetic (FM) dimer configurations. Energies and electronic structures were obtained by solving the Kohn-Sham equations self-consistently using the PBE1PBE hybrid functional potential [47–49] with the LanL2DZ basis set [50,51], in which core electrons are replaced by an effective core and only Zn^{2+} (4s, 3d, 4p), Se^{2-} (4s, 4p), Mn^{2+} (3s, 3p, 4s, 3d), and H (1s) atomic orbitals are described with explicit basis functions. This computational scheme has been successful in describing the electronic structures of $Zn_{1-x}TM_xO$ (where $TM = Co^{2+}$, Mn^{2+}) [43,52,53], $Cd_{1-x}Mn_xS$ [54], and $Cd_{1-x}Mn_xSe$ [55] nanocrystals. Convergence to the correct spin configuration was determined by analysis of the Mulliken spin density on each of the Mn^{2+} dopants. All molecular orbital plots were generated with an isosurface value of 0.035.

III. RESULTS AND ANALYSIS

A. TR-MCPL data and simulations

Figure 1(a) shows room-temperature electronic absorption and 1.7 K magnetoluminescence spectra of 1.5% (x = 0.015)

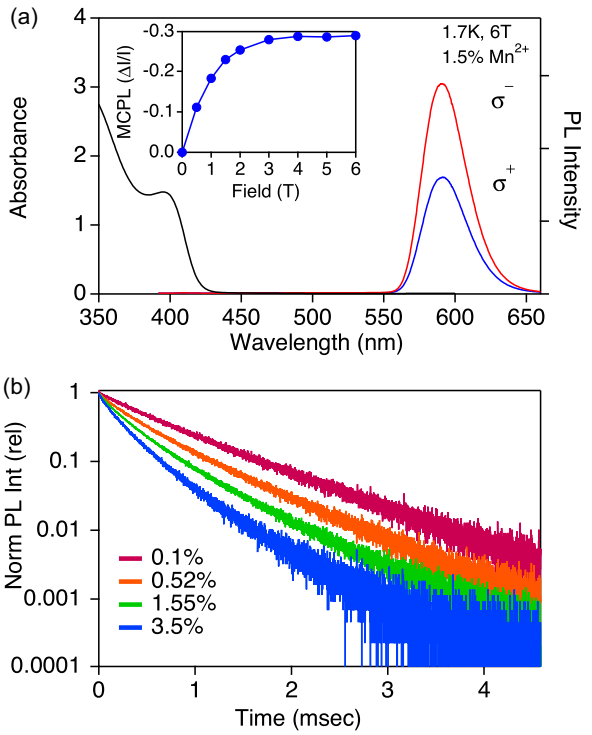

FIG. 1. (Color online) (a) Room-temperature absorption (left axis, black) and 1.7 K, 6 T magnetic circularly polarized luminescence spectra of 1.5% $Zn_{1-x}Mn_xSe/ZnS$ nanocrystals. Inset: Magnetic-field dependence of the MCPL ratio, $\Delta I/I$. (b) Room-temperature TR PL traces for $Zn_{1-x}Mn_xSe/ZnS$ NCs with Mn^{2+} concentrations from 0.1 to 3.5% as indicated. All nanocrystals have core $d \sim 3$ nm and shell thickness ~0.5 nm.

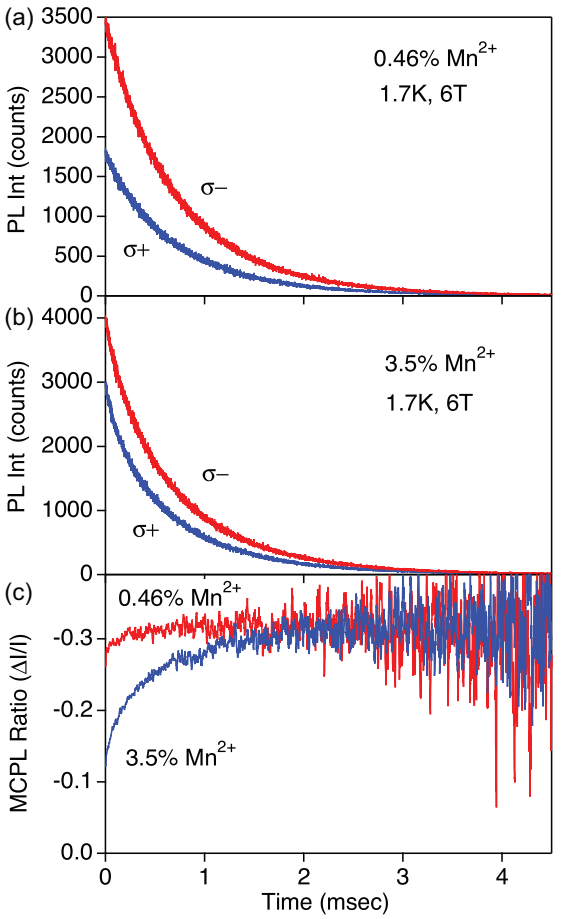

FIG. 2. (Color online) Time-resolved σ^+ and σ^- PL decay traces from (a) 0.46% and (b) 3.5% $Zn_{1-x}Mn_xSe/ZnS$ NCs (core $d = 3$ nm, respectively), both measured at 1.7 K, 6 T in the Faraday geometry. (c) Time-resolved MCPL ($\Delta I/I$ vs t) traces for the same samples measured under the same conditions.

$Zn_{1-x}Mn_xSe/ZnS$ NCs (core $d \sim 3$ nm, shell thickness ~0.5 nm). The absorption spectrum is dominated by the ZnSe core, with a first excitonic absorption maximum at ~400 nm. Luminescence spectra of the same sample show only the sensitized Mn^{2+} $^4T_1 \rightarrow {}^6A_1$ d-d band centered at ~590 nm. At low temperatures and in the presence of a magnetic field, this Mn^{2+} PL is partially circularly polarized, with greater σ^- intensity than σ^+ intensity. There was no detectable Zeeman splitting of the $^4T_1$ band (<~1 meV at 1.7 K and 6 T, see Supplemental Material [41]), and we were thus unable to confirm the recent report [12] of quantum-confinement-induced giant (5–10 meV) Zeeman splittings within the $^4T_1$ excited states of Mn^{2+} ions in quantum dots. $^4T_1$ Zeeman splittings of the magnitude proposed in Ref. [12] are not easily reconciled with the otherwise normal spectroscopic properties of Mn^{2+} ions in ZnSe QDs (PL decay time and energy, electron paramagnetic resonance [EPR] g value, etc.) and with the notion that this luminescent excited state is highly localized at the Mn^{2+} center. The inset to Fig. 1(a) plots the MCPL polarization ratio [$\Delta I/I$, as defined in Eq. (1)] vs applied magnetic field, measured at 1.7 K. Here, $\Delta I/I$ increases rapidly with applied field before leveling off between ~3 and 6 T at a value of $\Delta I/I \sim -0.30$. This value of $\Delta I/I$ is essentially identical to that measured for the same luminescence in bulk $Zn_{1-x}Mn_xS$ single crystals [56]

$$\Delta I/I = (I_+ - I_-)/(I_+ + I_-). \quad (1)$$

Figure 1(b) shows room-temperature PL decay traces measured for similar $Zn_{1-x}Mn_xSe/ZnS$ NCs containing various Mn^{2+} concentrations. At 0.1% Mn^{2+}, the PL decay is monoexponential with a lifetime of $\tau = 790$ μs. As the Mn^{2+} concentration increases to 3.5%, the decay accelerates and becomes multiexponential. At 3.5% Mn^{2+}, the time required to decay to $1/e$ of the initial intensity is 240 μs.

Figure 2(a) plots decay traces for the 590 nm PL of 0.46% $Zn_{1-x}Mn_xSe/ZnS$ NCs, measured at 1.7 K in a 6 T magnetic field (Faraday geometry) and resolved into σ^+ and σ^- components. Both circular polarizations show monoexponential decay with $\tau = 720$ μs. Figure 2(b) shows PL decay traces measured for 3.5% $Zn_{1-x}Mn_xSe/ZnS$ NCs under the same conditions. These decay traces are multiexponential but are both fit reasonably well to two exponentials with time constants of 750 and 160 μs. Unlike the traces in Fig. 2(a), the σ^+ and σ^- decay traces of the 3.5% $Zn_{1-x}Mn_xSe/ZnS$ NCs do not overlay one another when normalized, a difference highlighted by plotting $\Delta I/I$ vs time as shown in Fig. 2(c). For the 0.46% Mn^{2+} sample, $\Delta I/I$ is nearly constant at about -0.31. In contrast, the 3.5% Mn^{2+} NCs show a pronounced evolution of $\Delta I/I$ from ~-0.15 at short times to ~-0.31

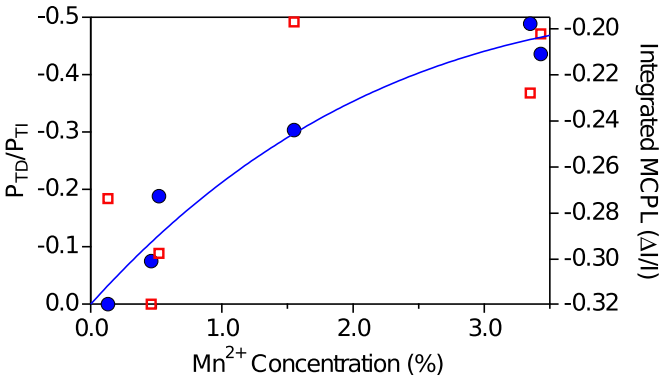

FIG. 3. (Color online) Mn^{2+} concentration dependence of P_{TD}/P_{TI} (left axis, blue circles) and time-integrated $\Delta I/I$ (right axis, red squares), measured at 1.7 K and 6 T. Note the negative axes. The solid curve plots the calculated probability that a Mn^{2+} ion is part of a nearest-neighbor dimer, scaled arbitrarily to overlay the data. The solid curve runs from zero at 0% Mn^{2+} to 0.22 at 3.5% Mn^{2+}.

at times longer than ~2 ms. The smaller $\Delta I/I$ at short times implicates a subset of luminescent Mn^{2+} ions that emit on a faster timescale with a less negative (or possibly even positive) polarization ratio. As detailed below, this subset can be identified as luminescent exchange-coupled Mn^{2+}-Mn^{2+} dimers. For quantitative analysis, we define the magnitude of the time-independent MCPL polarization (P_{TI}) as the long-time asymptote of $\Delta I/I$ ($t > 2.5$ ms, experimentally) and the magnitude of the time-dependent MCPL polarization (P_{TD}) as the difference between $\Delta I/I$ at $t = 0$ and P_{TI}, as described by Eqs. (2a) and (2b). For the 3.5% Mn^{2+} sample of Fig. 2, $P_{TI} = -0.30$, $P_{TD} = +0.15$, and $P_{TD}/P_{TI} = -0.50$

$$P_{TI} = \left(\frac{\Delta I}{I}\right)_{t\to\infty}, \tag{2a}$$

$$P_{TI} = \left(\frac{\Delta I}{I}\right)_{t=0} - P_{TI}. \tag{2b}$$

Figure 3 plots P_{TD}/P_{TI} vs Mn^{2+} concentration for a series of $Zn_{1-x}Mn_xSe/ZnS$ NCs. Increasing from the low-Mn^{2+} limit up to 3.5% Mn^{2+}, P_{TD}/P_{TI} grows sublinearly from zero to ~−0.50. Figure 3 also plots time integrated (CW; continuous wave) 1.7 K, 6 T MCPL ratios vs Mn^{2+} concentration for the same samples. Here, $\Delta I/I$ decreases from about −0.30 at <1% Mn^{2+} to −0.20 at >3% Mn^{2+} (note the negative scale), roughly in proportion to P_{TD}/P_{TI} but with substantially greater scatter among the data points. These trends are interpreted as reflecting dimer formation as Mn^{2+} concentrations increase. If Mn^{2+} were distributed statistically over the available ZnSe cation sites, the probability D of a given Mn^{2+} ion being part of an isolated nearest-neighbor Mn^{2+}-Mn^{2+} dimer would be roughly $D = 12x(1-x)^{18}$ [57]. Between 0 and 3.5% Mn^{2+}, D increases sublinearly from zero to ~0.22. The solid line in Fig. 3 plots D vs Mn^{2+} concentration, scaled vertically to approximate the MCPL data. The curvature of D reproduces the experimental data well, supporting the conclusion that Mn^{2+}-Mn^{2+} dimer formation is responsible for these changes in time-dependent and CW MCPL signals with increasing Mn^{2+} concentration. As a corollary, the agreement found in Fig. 3 suggests that the individual monomer and dimer MCPL polarization ratios are not significantly concentration dependent.

To analyze the MCPL time dependence, we describe the time dependence of $\Delta I/I$ as arising from a superposition of time-dependent monomer and dimer emission with static polarizations, as in Eq. (3)

$$\frac{\Delta I}{I}(t) = \frac{I_m(t)\cdot\left(\frac{\Delta I}{I}\right)_m + I_d(t)\cdot\left(\frac{\Delta I}{I}\right)_d}{I_m(t)+I_d(t)}. \tag{3}$$

Here, $I_m(t)$ and $I_d(t)$ denote decaying luminescence intensities of monomers (m) and dimers (d), respectively, and $(\Delta I/I)_m$ and $(\Delta I/I)_d$ refer to the individual time-independent MCPL polarization ratios of each. Because photoexcited dimers decay faster than photoexcited monomers, $\Delta I/I(t)$ converges to $(\Delta I/I)_m$ at long times. Normalizing the total intensity at $t = 0$ and assuming crudely that all luminescence comes from either monomers or dimers [$I_m(0) + I_d(0) = 1$], Eq. (3) simplifies to Eq. (4) at $t = 0$

$$\frac{\Delta I}{I}(0) = [1 - I_d(0)]\cdot\left(\frac{\Delta I}{I}\right)_m + I_d(0)\cdot\left(\frac{\Delta I}{I}\right)_d. \tag{4}$$

The experimental quantities P_{TD} and P_{TI} can now be expressed in terms of these same parameters, as shown in Eqs. (5a) and (5b)

$$P_{TI} = \left(\frac{\Delta I}{I}\right)_{t\to\infty} = \left(\frac{\Delta I}{I}\right)_m, \tag{5a}$$

$$P_{TD} = \left(\frac{\Delta I}{I}\right)_{t=0} - P_{TI} = I_d(0)\left[\left(\frac{\Delta I}{I}\right)_d - \left(\frac{\Delta I}{I}\right)_m\right]. \tag{5b}$$

Here, P_{TD} (as well as P_{TD}/P_{TI}) is therefore directly proportional to $I_d(0)$ (the intensity of dimer emission at $t = 0$). Under the assumption that monomer and dimer MCPL ratios and relative quantum yields are concentration independent over this limited range of concentrations, $I_d(0)$ is proportional to D. Note also that $(\frac{\Delta I}{I})_d - (\frac{\Delta I}{I})_m$ is the only magnetic-field-dependent term in Eq. (5b). These equations now allow a quantitative analysis of the experimental TR-MCPL results.

Figure 4(a) plots the magnetic-field dependence of the TR-MCPL measured for the 0.52% Mn^{2+} sample from 0 to 4.5 T at 1.7 K. At zero magnetic field, $\Delta I/I(t) = 0$ at all times. As the field is applied, P_{TI} becomes progressively larger, eventually leveling off at ~−0.38. This result is similar to that observed in the CW MCPL at small x and confirms assignment of the long-time MCPL to Mn^{2+} monomers. Here, P_{TD} also becomes more pronounced with increasing magnetic field. Samples with 1.5% and 3.5% Mn^{2+} show similar trends. Figure 4(a) plots the magnetic-field dependence of P_{TD} and P_{TI} for the 0.52% Mn^{2+} sample, both normalized in the linear (Curie) region of the saturation magnetization. The dashed curves in Fig. 4(b) show 1.7 K, $g = 2$ Brillouin magnetization curves calculated using Eq. (6) for various hypothetical spin states, assuming $g = 2.0$. Here, μ_B is the Bohr magneton, k is the Boltzmann constant, and N is a scaling factor

$$M(H) = \frac{1}{2}Ng\mu_B\left\{(2S+1)\cdot\coth\left[(2S+1)\cdot\frac{g\mu_B H}{2kT}\right] - \coth\left(\frac{g\mu_B H}{2kT}\right)\right\}. \tag{6}$$

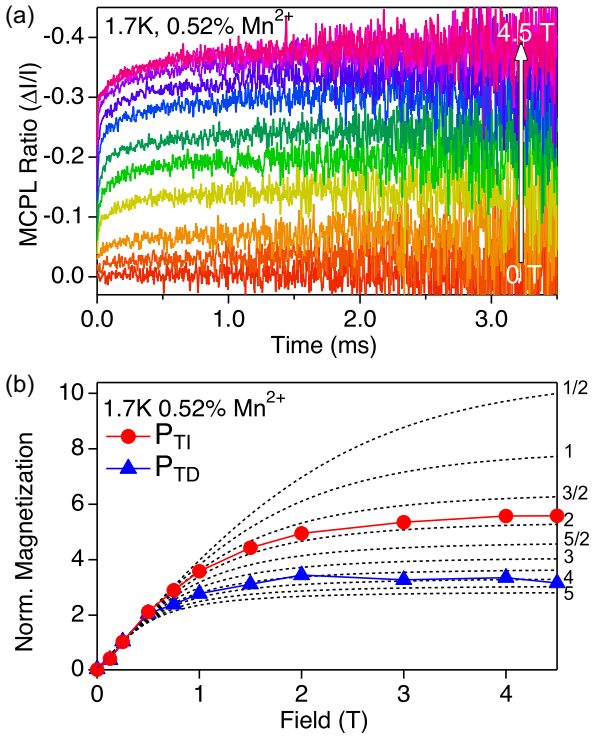

FIG. 4. (Color online) (a) Time-resolved MCPL of 0.52% $Zn_{1-x}Mn_xSe/ZnS$ NCs, measured from 0 to 4.5 T at 1.7 K. (b) P_{TD} (blue triangle) and P_{TI} (red circle) values from the traces in (a) plotted vs applied magnetic field and normalized at 0.25 T. The dashed lines plot Brillouin magnetization functions calculated for $S = 1/2$ to 5 ($g = 2$, 1.7 K), also normalized at 0.25 T.

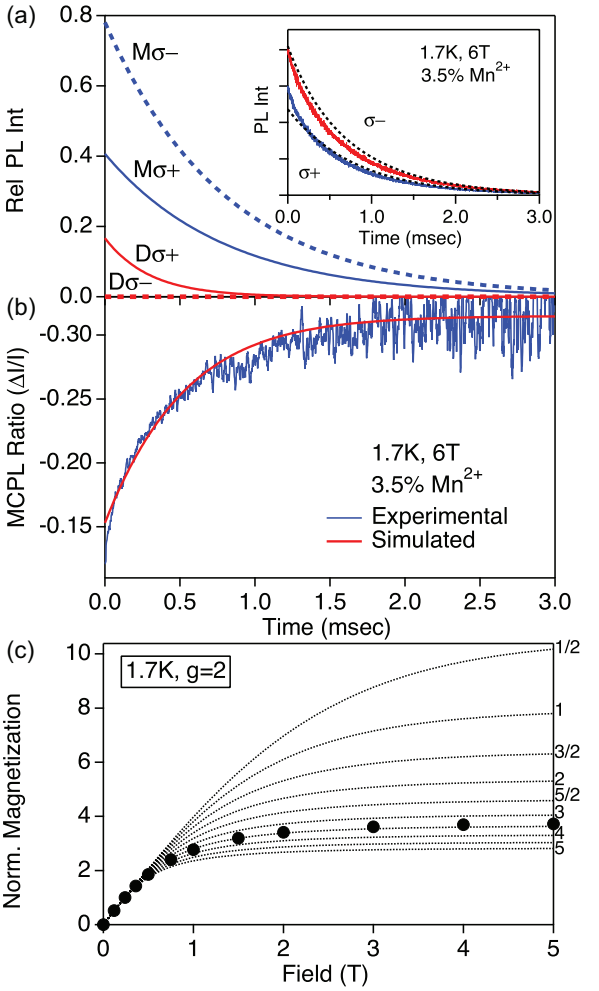

FIG. 5. (Color online) (a) Simulated circularly polarized PL decay curves for monomers [blue, $\tau_m = 800$ μs, $(\Delta I/I)_m = -0.32$] and dimers [red, $\tau_d = 300$ μs, $(\Delta I/I)_d = +1.00$). Here, σ^- and σ^+ components are shown as dashed and solid lines, respectively. The integrated dimer PL accounts for 5% of the overall PL in this simulation. Inset: The simulated summed σ^- and σ^+ PL intensities overlaid with the experimental data from Fig. 2(b). (b) The simulated MCPL ratio from (a) as a function of time (solid red line), overlaid with the experimental data from Fig. 2(c). (c) Simulated magnetic field dependence of P_{TD} obtained by scaling the monomer and dimer MCPL polarization ratios by the $S = 3/2$ and $S = 4$ Brillouin functions, respectively.

For comparison with the experimental data in Fig. 4(b), these Brillouin curves have also been normalized at 0.25 T. Such normalization emphasizes the different curvatures of the saturation magnetization of different spin states, with the highest spin states saturating at the lowest magnetic fields and normalized magnetization magnitudes. When plotted in this way, the saturation value of P_{TI} is significantly greater than that for P_{TD}, suggesting that P_{TD} arises from a luminescent state with a greater net spin [58]. Specifically, the P_{TI} data resemble an $S = 3/2$ state, consistent with this luminescence coming from the Mn^{2+} $^4T_1$ excited state, but the P_{TD} data most closely resemble the $S = 4$ Brillouin function. This analysis strongly suggests that dimers luminesce from a high-spin excited state.

Equations (3)–(5) were used to simulate both the TR-MCPL and saturation magnetization data, and the results are summarized in Fig. 5. Simulations of the 3.5% Mn^{2+} TR-MCPL data of Figs. 2(b) and 2(c) are described here because P_{TD} is most prominent in these data. Although the PL decay curves in Figs. 1 and 2 are nonexponential for this sample, the simulations were performed using the simplifying assumptions that (a) all monomers decay with the same exponential lifetime as measured in the lowest concentration sample ($\tau_m = 800$ μs) and show the same MCPL ratio [$(\Delta I/I)_m = -0.32$ at saturation, with $S = 3/2$ magnetization], and (b) all dimers also decay with the same single exponential lifetime. Thus, the model's variable parameters are dimer PL lifetime, the fraction of photons emitted from dimers, the dimer spin state (which was assumed to be $\leqslant 4$), and $(\Delta I/I)_d$. As detailed below, the individual TR-MCPL decay curves alone could be simulated by many combinations of those four parameters, but their magnetic field dependence could only be reproduced with $S = 4$ and $(\Delta I/I)_d \sim +1.0$ at 4.5 T, i.e. essentially complete circular polarization, providing a unique set of viable simulation parameters for both experiments. With these parameters, photoexcited dimers account for ~5% of the total integrated PL for this sample and decay with $\tau_d = 300$ μs.

The inset to Fig. 5(a) plots σ^+- and σ^--polarized PL decay traces simulated using the above parameters, overlaid with the experimental data from Fig. 2(b). The simulated σ^+ and σ^- PL decay traces reproduce the experimental data well. For

illustration of the various monomer and dimer contributions, the main panel of Fig. 5(a) plots the four individual σ^+- and σ^--polarized PL decay traces calculated from these simulation parameters. Figure 5(b) plots the simulated TR-MCPL trace [$\Delta I/I(t)$ vs t] along with the experimental TR-MCPL data from Fig. 2(c). The simulated TR-MCPL curve also agrees well with the experimental data. A noteworthy observation from this analysis is that the apparent decay time of P_{TD} ($\sim$600 μs) does not match the dimer decay time ($\tau_d = 300$ μs), but rather is the weighted average of this and the monomer decay time, as described by Eq. (3).

Figure 5(c) plots the simulated magnetic field dependence of P_{TD}, for comparison with the experimental data in Fig. 4(b). As noted in the discussion of Eq. (5b), the field dependence of P_{TD} is only sensitive to the values of S and $(\Delta I/I)$, and not to emission intensities or lifetimes. Because S_m and $(\Delta I/I)_m$ are known from the low-concentration limit, S_d and $(\Delta I/I)_d$ are the only unknown parameters. To simulate the TR-MCPL magnetic field dependence, 1.7 K monomer and dimer TR-MCPL traces were calculated for each magnetic field by scaling $(\Delta I/I)_m$ and $(\Delta I/I)_d$ at each field by their respective Brillouin magnetization functions [Eq. (6), $S_m = 3/2$ and $S_d \leqslant 4$]. From these simulated traces, P_{TD} was then determined at each field by the same methods used to analyze the experimental TR-MCPL data, and the resulting curve was normalized at 0.25 T as in Fig. 4. The experimental data could only be reproduced with $S_d = 4$ and $(\Delta I/I)_d \sim +1.0$. This dimer MCPL ratio in turn defines a unique set of simulation parameters for the full model, necessitating that dimers account for $\sim$5% of the total integrated PL. This fraction is smaller than $D \sim 22\%$ based on Mn^{2+} concentration, a difference that could have many origins including poorer sensitization or smaller PL quantum yields for the dimers.

B. Interpretation of the sign and purity of the dimer MCPL

From the simulations summarized in Fig. 5, the magnetic-field dependence of P_{TD} implies that dimer MCPL is $\sim$100% circularly polarized, with the opposite sign of the monomer MCPL. Figure 6 illustrates the proposed origin of this purely σ^+ polarization schematically. Assuming a cubic spin-only picture for illustrative purposes, magnetized monomers at low temperatures luminesce from only the $m_s = -3/2$ Zeeman component of the $^4T_1$ excited state. In the Faraday geometry, only transitions with $\Delta m_s = \pm 1$ are allowed, yielding right (σ^+) and left (σ^-) circularly polarized luminescence, respectively. The monomer MCPL ratio is therefore defined by the relative probabilities of the $m_s = -3/2 \rightarrow -5/2$ (σ^-) and $m_s = -3/2 \rightarrow -1/2$ (σ^+) transitions, which are different for nontrivial reasons [56]. In exchange-coupled Mn^{2+}-Mn^{2+} dimers, however, the total luminescence is dominated by spin-allowed ($\Delta S = 0$) components of the dimer spin ladder, as per the Tanabe mechanism. As illustrated in Fig. 6, luminescence from a ferromagnetically coupled ($S = 4$) dimer excited state is thus dominated by transitions to the $S = 4$ dimer ground state. From Fig. 6, MCPL from the fully magnetized $S = 4$ dimer excited state originates from the $m_s = -4$ Zeeman sublevel and can only occur with $\Delta m_s = +1$, because no $\Delta m_s = -1$ transition to the $S = 4$ ground state

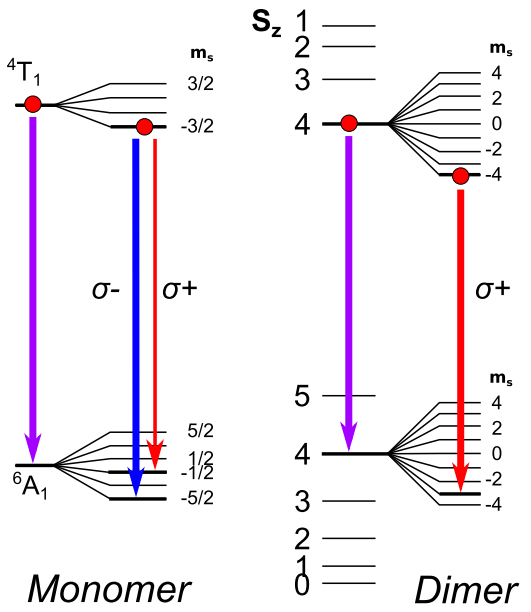

FIG. 6. (Color online) Schematic depictions of the transitions defining MCPL ratios for monomers and dimers in $Zn_{1-x}Mn_xSe$ and related systems in the spin-only limit. In monomers (left), MCPL is determined by the relative transition moment probabilities of $\Delta m_s = -1$ (σ^-, blue arrow) and $\Delta m_s = +1$ (σ^+, red arrow). In dimers (right), the ground state is antiferromagnetically coupled, and the luminescent excited state is ferromagnetically coupled. The dimer luminescence intensity is dominated by the spin-allowed $\Delta S = 0$ transition. In the dimer MCPL, only the $\Delta m_s = +1(\sigma^+)$ component of this transition conserves angular momentum, leading to 100% circular polarization with the opposite sign as in the monomers. Splittings are not to scale.

is available (i.e. no $m_s = -5$ component of this state exists). Therefore, to the extent that the overall PL is dominated by the $\Delta S = 0$ dimer transition, the MCPL from coupled Mn^{2+}-Mn^{2+} dimers is purely σ^+ circularly polarized. Although Jahn-Teller distortions and spin-orbit coupling undoubtedly make the actual luminescent excited states of both monomers and dimers more complicated than illustrated in Fig. 6, these spin-only pictures capture the essence of the experimental observations.

C. Interpretation of the sign of Mn^{2+}-Mn^{2+} excited-state superexchange coupling

The change in sign of the Mn^{2+}-Mn^{2+} dimer magnetic-exchange coupling constant upon photoexcitation can be understood by evaluating the available microscopic superexchange pathways in the dimer ground and excited states. Figure 7(a) illustrates the d electrons of two coupled tetrahedral Mn^{2+} ions schematically. When both Mn^{2+} ions are in their $^6A_1$ ground states ($|^6A_1, ^6A_1\rangle$), all five d orbitals of each ion are singly occupied. In this configuration, Pauli exclusion dictates that partial spin transfer from one Mn^{2+} to the other can only occur if the electrons on each Mn^{2+} have the opposite spin, i.e. only antiferromagnetic superexchange pathways exist. In the luminescent $|^4T_1, ^6A_1\rangle$ excited state of the dimer, however, one of the Mn^{2+} ions has an $e^3t_2^2$ configuration involving an unoccupied t_2 orbital and a doubly occupied e orbital. Spin transfer from a half-full to an empty

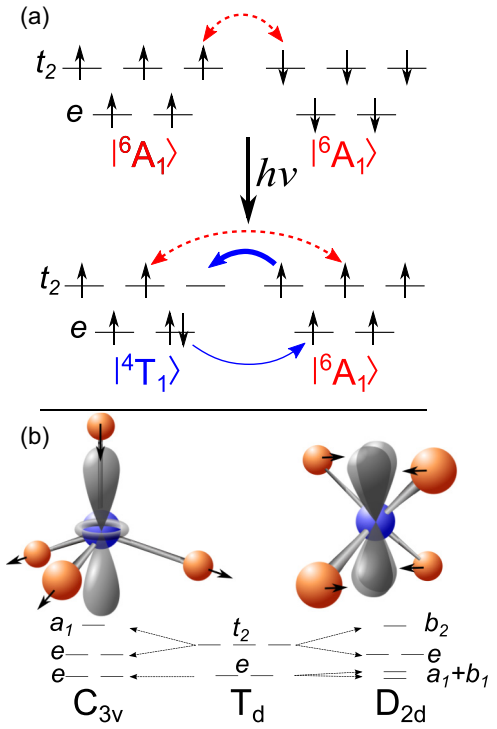

FIG. 7. (Color online) (a) Schematic summary of spin-transfer processes responsible for ground- and excited-state magnetic exchange coupling of Mn^{2+}-Mn^{2+} dimers in ZnSe. The dashed red arrows denote spin-transfer processes favoring antiferromagnetic Mn^{2+}-Mn^{2+} coupling, and the solid blue arrows denote spin-transfer processes favoring ferromagnetic coupling. (b) Two possible Jahn-Teller distortions of the Mn^{2+} $^4T_1$ excited state (C_{3v} and D_{2d}), and the corresponding d-orbital splitting patterns.

t_2 orbital favors net parallel (ferromagnetic) alignment of the Mn^{2+} spins, as illustrated by the thick blue arrow in Fig. 7(a) for the $|^4T_1,^6A_1\rangle$ dimer excited state. Similarly, spin transfer from the doubly occupied e orbital to a half-occupied orbital on the other Mn^{2+} [thin blue arrow in Fig. 7(a)] also favors parallel spin alignment, but at this stage, e-based pathways are neglected for simplicity under the assumption that their interactions are much weaker. At the same time, other antiferromagnetic pathways similar to those of the dimer ground state may still exist [dashed arrows in Fig. 7(a)]. Because ferromagnetic and antiferromagnetic pathways are both available in the $|^4T_1,^6A_1\rangle$ dimer excited state, the sign of the overall exchange coupling constant depends on the relative strengths of the active exchange pathways, which in turn primarily reflect overlap of the pertinent d orbitals with the valence orbitals of the bridging selenide. From the observation of net ferromagnetic Mn^{2+}-Mn^{2+} coupling in the luminescent dimer excited state, we conclude that the empty t_2 orbital must have substantial overlap with the bridging Se^{2-} mediating the superexchange.

Dimer exchange interactions can be assessed more quantitatively using perturbation methods. The exchange interaction between two ions A and B is formulated in terms of the Heisenberg–Dirac–van Vleck effective Hamiltonian shown in Eq. (7)

$$\hat{H} = -2J_{dd}\hat{S}_A \cdot \hat{S}_B. \tag{7}$$

Here, J_{dd} is the exchange coupling constant and $\hat{S}_A, \hat{S}_B$ represent the Mn^{2+} spin operators. Experimentally, the ground-state coupling constant of Mn^{2+}-Mn^{2+} dimers in ZnSe is $J_{dd} \approx -1.0$ meV, i.e. antiferromagnetic [33,59]. This coupling constant can be described with reasonable accuracy using fourth-order perturbation theory [60]. Interestingly, similar perturbation calculations performed for Cr^{2+}-Cr^{2+} dimers in ZnSe predict that ferromagnetic coupling may be possible in these dimers under certain circumstances [61]. Cr^{2+} has an $e^2t_2^2$ electronic configuration, and hence has ferromagnetic superexchange pathways analogous to the t_2-t_2 ferromagnetic pathway of the Mn^{2+} $^4T_1$ excited state illustrated in Fig. 7(a). Notably, the magnitude and even the sign of the Cr^{2+}-Cr^{2+} dimer exchange coupling was predicted to be sensitive to the Cr^{2+} Jahn-Teller distortion [61].

To assess the superexchange coupling in the $|^4T_1,^6A_1\rangle$ Mn^{2+}-Mn^{2+} dimer excited state, we take a similar fourth-order perturbation approach, based on the formalism developed by Weihe and Güdel for molecular transition-metal dimers [62–64]. Details of these calculations are provided in the Supplemental Material [41]. From the perturbation formalism, the most sensitive parameter determining the strength of an individual superexchange pathway is the overlap of the relevant d orbital with the bridging ligand valence orbitals, which determines that pathway's transfer integral. Calculation of the pathway-specific transfer integrals for the Mn^{2+}-Mn^{2+} excited state is exceedingly difficult because of the Jahn-Teller distortion of this excited state. We therefore calculate two extreme scenarios for illustrative purposes: (i) the nine individual t_2-t_2 transfer integrals are all equal to the average transfer integral, and (ii) superexchange proceeds solely through a single dominant t_2-t_2 pathway whose transfer integral is therefore nine times the average. For simplicity, we neglect pathways involving the e orbitals, and we estimate the excited-state transfer integrals from the ground-state exchange coupling strength, neglecting changes due to overall bond-length contraction upon photoexcitation. Because the transfer integral is the only unknown parameter in these calculations, it can be fixed to reproduce the experimental ground-state coupling constant and then used to predict the excited-state coupling.

In the limit where ground-state superexchange proceeds through nine equivalent t_2-t_2 pathways, the experimental ground-state $J_{dd} \approx -1.0$ meV implies an average transfer integral of 0.6 eV. Applying this transfer integral to the dimer excited state, the six remaining antiferromagnetic pathways contribute -0.4 meV each, and the three ferromagnetic pathways contribute $+0.05$ meV each, to yield an overall coupling constant of $J_{dd}(\mathrm{ES}) \sim -2.5$ meV (antiferromagnetic). This scenario is thus inconsistent with the experimental observation of ferromagnetic excited-state coupling, from which we conclude that ferromagnetic superexchange pathways must play a greater-than-average role.

In the limit of just one active superexchange pathway, the experimental ground-state J_{dd} implies a transfer integral of 1.0 eV. If upon photoexcitation, the empty orbital does not participate in the dominant superexchange pathway, then the

excited-state superexchange remains antiferromagnetic, and the reduced charge-transfer energy increases the magnitude of J_{dd}(ES) to ∼−3.6 meV. On the other hand, if photoexcitation removes an electron from the d orbital involved in the principal superexchange pathway, then the excited-state superexchange is ferromagnetic with J_{dd}(ES) ∼ +0.4 meV. This result qualitatively supports the conclusion that the empty t_2 orbital of the photoexcited Mn^{2+} ion must be directed at the bridging selenide such that it dominates the excited-state Mn^{2+}-Mn^{2+} superexchange.

We hypothesize that the Jahn-Teller distortion of the $^4T_1$ excited state, which splits the d orbital degeneracies, plays an important role in orienting the empty t_2 orbital for effective ferromagnetic superexchange. Figure 7(b) illustrates two of the possible Jahn-Teller distortions of the $^4T_1$ excited state [65]. In Fig. 7(b) (left), Mn^{2+} undergoes a C_{3v} distortion involving contraction along the Mn^{2+}-Se^{2-} (bridge) axis, orienting the empty a_1 orbital for effective superexchange. In Fig. 7(b) (right), Mn^{2+} undergoes a D_{2d} distortion involving dihedral compression and positioning the empty b_2 orbital for effective superexchange. These distortions would not only favor a single superexchange pathway, but would also increase the overlap integral for the one destabilized (empty) orbital, thereby increasing the magnitude of J_{dd}. A more detailed description of the Jahn-Teller effect in the luminescent Mn^{2+} $^4T_1$ excited state will be presented elsewhere [66].

D. Density functional theory calculations

Additional insight into the excited-state Mn^{2+}-Mn^{2+} exchange coupling is obtained from DFT calculations. The energies of $Zn_{84}Mn_2Se_{86}$ nanocrystals containing Mn^{2+}-Mn^{2+} dimers in their ground state and first electronic excited states were calculated for scenarios in which the dimer spins were forced to align either ferromagnetically or antiferromagnetically. The energy difference between these two cases was then used to calculate J_{dd} according to Eqs. (8a) and (8b), which reflect the energies of the $S = 0 \rightarrow 5$ (GS) and $S = 0 \rightarrow 4$ (ES) Landé spin ladders

$$J_{dd}^{GS} = \frac{E_{AFM}^{GS} - E_{FM}^{GS}}{30}, \tag{8a}$$

$$J_{dd}^{ES} = \frac{E_{AFM}^{ES} - E_{FM}^{ES}}{18}. \tag{8b}$$

All total-energy calculations were performed after complete geometry optimization, which accounts for changes in cation site symmetry, orbital overlap, and hence exchange energies upon relaxation of the electronically excited Mn^{2+} ion. For the ground state, the value of J_{dd} calculated in this way is −0.68 meV, which agrees reasonably well with the experimental value (∼−1.0 meV) [18,33,59]. In the dimer excited state, the ferromagnetic configuration was found to be more stable than the antiferromagnetic configuration by 24.5 meV, corresponding to J_{dd} = +1.36 meV [Eq. (8b)]. Density functional theory calculations thus predict net ferromagnetic exchange in the luminescent excited states of Mn^{2+}-Mn^{2+} dimers, in agreement with experiment.

Figure 8 shows density of states (DOS) diagrams calculated for the antiferromagnetically coupled Mn^{2+}-Mn^{2+} ground state ($|^6A_1,^6A_1\rangle$) and the ferromagnetically coupled

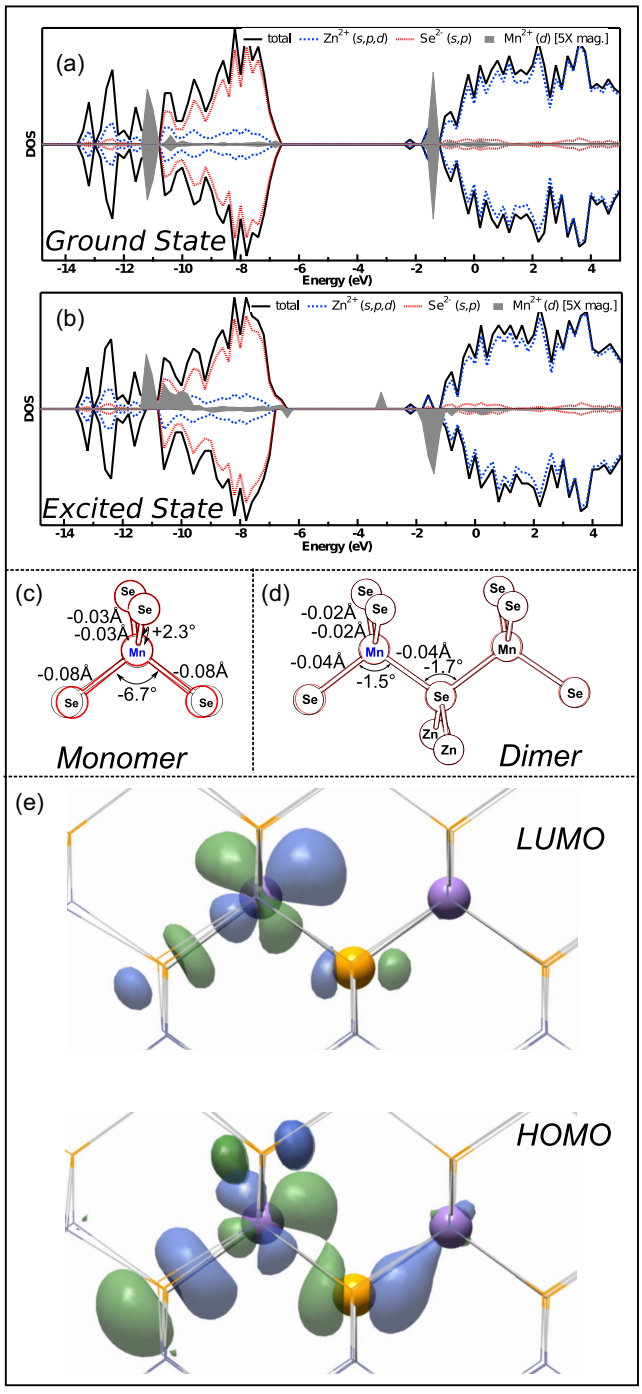

FIG. 8. (Color online) Results from DFT calculations on $Zn_{84}Mn_2Se_{86}$ nanocrystals. Density of states diagrams for (a) the antiferromagnetically coupled $|^6A_1,^6A_1\rangle$ ground state and (b) the ferromagnetically coupled $|^4T_1,^6A_1\rangle$ excited state. The top and bottom of each plot denote α and β spins, respectively. (c) and (d) Structural changes upon photoexcitation of Mn^{2+} monomer and Mn^{2+}-Mn^{2+} dimer. Ground-state (black) and excited-state (red) structures are illustrated, and the most significant changes in bond lengths and angles upon excitation are indicated. (e) Electron density contours of the Mn^{2+}-Mn^{2+} dimer LUMO and HOMO in the ferromagnetically coupled $|^4T_1,^6A_1\rangle$ excited state, which correspond primarily to the empty and doubly occupied orbitals of the photoexcited Mn^{2+} ion, respectively. Mn^{2+} ions are shown in purple, Zn^{2+} in blue, and Se^{2-} in yellow.

Mn^{2+}-Mn^{2+} excited state ($|^4T_1,^6A_1\rangle$). In the ground state [Fig. 8(a)], antiferromagnetic coupling gives a symmetrical spin population with no net spin ($S = 0$). In the excited state [Fig. 8(b)], the spin projection of the dimer is no longer symmetrical. Specifically, new β spin density appears near the valence band edge (the spin-down e electron), and the empty spin-up t_2 orbital now resides within the ZnSe gap. Additionally, the d orbital manifolds are broadened relative to the ground state, reflecting splittings due to low-symmetry structural relaxation.

Figure 8(c) shows the calculated distortion upon excitation of an isolated Mn^{2+} ion to its $^4T_1$ state. All four Mn^{2+}-Se^{2-} bonds contract because of depopulation of a t_2 antibonding orbital, but two of the bonds contract more than the other two, breaking the T_d cation symmetry. This distortion resembles a partner function of the Jahn-Teller-active T_2 stretching coordinate, in which two bonds contract and two elongate. A similar distortion is calculated for the excited Mn^{2+} in the $|^4T_1,^6A_1\rangle$ dimer excited state [Fig. 8(d)], but the distortions appear smaller. Importantly, one of the shortened bonds is to the bridging Se^{2-}, indicating the depopulated t_2 orbital is directed toward this Se^{2-}, favoring ferromagnetic Mn^{2+}-Mn^{2+} superexchange coupling (Sec. IIIC).

Figure 8(e) [lowest unoccupied molecular orbital (LUMO)] shows a contour plot depicting this empty orbital in the dimer excited state. This empty orbital indeed shows a substantial σ-type antibonding interaction with the bridging Se^{2-} p orbital, reflecting the primary ferromagnetic superexchange pathway of the luminescent $|^4T_1,^6A_1\rangle$ excited state. Details of the excited-state distortions, and contour plots for all 20 d-based dimer orbitals, are provided in the Supplemental Material [41].

An interesting result from the DFT calculations is that the highest occupied molecular orbital (HOMO) is also significantly hybridized with the bridging Se^{2-} in the $|^4T_1,^6A_1\rangle$ excited state [Fig. 8(e) (HOMO)]. This covalency arises from the relatively high energy of this β-spin electron [Fig. 8(b)] because of the single-site Coulomb interaction, and it implies a significant contribution to excited-state magnetic exchange coupling involving this HOMO. This interaction was neglected in the perturbation treatment of Sec. IIIC because of the smaller metal-ligand overlap of the cubic e orbitals. Importantly, superexchange involving this orbital also stabilizes the ferromagnetic configuration of Mn^{2+}-Mn^{2+} dimer spins [64].

Overall, the DFT calculations predict ferromagnetic exchange coupling in the first electronic excited state of Mn^{2+}-Mn^{2+} dimers in ZnSe, in agreement with experiment. The DFT calculations illustrate symmetry-reducing Jahn-Teller distortions in the first excited states of Mn^{2+} monomers and Mn^{2+}-Mn^{2+} dimers in ZnSe, which in the latter promote overlap of the empty d orbital of t_2 parentage with the bridging Se^{2-}, in good agreement with expectations from perturbation analysis. The DFT calculations further suggest an additional effective ferromagnetic exchange pathway involving the excited-state HOMO.

IV. SUMMARY

The excited-state magnetism of photoexcited Mn^{2+}-Mn^{2+} dimers in $Zn_{1-x}Mn_xSe$ nanocrystals has been investigated using TR-MCPL spectroscopy. These experiments reveal ferromagnetic exchange coupling in the luminescent $|^4T_1,^6A_1\rangle$ electronic excited state of Mn^{2+}-Mn^{2+} dimers, in contrast with the antiferromagnetic exchange coupling universally observed in the $|^6A_1,^6A_1\rangle$ ground states of Mn^{2+}-Mn^{2+} dimers in ZnSe and related semiconductors. Perturbation theory and DFT calculations indicate that this change in the sign of J_{dd} derives primarily from a ferromagnetic superexchange pathway involving spin transfer into the empty t_2 orbital of the excited Mn^{2+} ion. Both perturbation and DFT analyses indicate that this empty t_2 orbital has a lobe oriented toward the bridging Se^{2-}, well situated for effective ferromagnetic superexchange. Ferromagnetic superexchange involving the doubly occupied e orbital in the dimer excited state is also suggested by DFT calculations. This new information about the magnetic properties of photoexcited Mn^{2+}-Mn^{2+} dimers in II-VI semiconductors appears to resolve a longstanding question in the literature and may warrant revisiting the assignment of single crystal absorption and emission spectra for this class of materials.

The observation of ferromagnetic exchange coupling within the excited states of Mn^{2+}-Mn^{2+} dimers in ZnSe could potentially have interesting ramifications for optically switchable magnetism in semiconductors relevant to spin electronics. Although the materials investigated here are not immediately applicable for optical switching, the sensitized $S = 0 \rightarrow 4$ photoexcitation within a semiconductor, combined with the 100% circularly polarized luminescence of this excited state under a magnetic field, is highly attractive for further investigation in this regard. For example, future synthetic advances may open routes to materials containing only dimers or related small clusters [67]. In such materials, these photoinduced spin-state changes would manifest themselves as giant Zeeman splittings of the semiconductor band structure in ways that could be useful for optically triggered spin filtering or spin transduction applications.

ACKNOWLEDGMENTS

The authors thank Alina Schimpf for valuable assistance. Financial support from the U.S. National Science Foundation (DMR-1206221 to D.R.G., CHE-1265945 to X.L., American Competitiveness in Chemistry Postdoctoral Fellowship to J.L.D.) is also gratefully acknowledged. Part of this work was conducted at the University of Washington NanoTech User Facility, a member of the NSF National Nanotechnology Infrastructure Network (NNIN).

[1] N. A. Vlasenko and Y. A. Popkov, Opt. Spektrosk. **8**, 81 (1960).
[2] R. Beaulac, S. T. Ochsenbein, and D. R. Gamelin, in *Semiconductor Quantum Dots*, edited by V. I. Klimov (CRC Press, Boca Raton, FL, 2010), p. 397.
[3] K. Shibata, E. Nakayama, I. Souma, A. Murayama, and Y. Oka, Phys. Status Solidi B **229**, 473 (2002).
[4] C. Ronda (ed.), *Luminescence: From Theory to Applications* (Wiley-VCH, Weinheim, Germany, 2008).

[5] H.-Y. Chen, T.-Y. Chen, and D. H. Son, J. Phys. Chem. C **114**, 4418 (2010).

[6] T. Toyama, D. Adachi, M. Fujii, Y. Nakano, and H. Okamoto, J. Non-Cryst. Sol. **299–302**, 1111 (2002).

[7] H. Yang, P. H. Holloway, and B. B. Ratna, J. Appl. Phys. **93**, 586 (2003).

[8] V. Wood, J. E. Halpert, M. J. Panzer, M. G. Bawendi, and V. Bulović, Nano Lett. **9**, 2367 (2009).

[9] C. S. Erickson, L. R. Bradshaw, S. McDowall, J. D. Gilbertson, D. R. Gamelin, and D. L. Patrick, ACS Nano (to be published), doi: 10.1021/nn406360w.

[10] S. E. Irvine, T. Staudt, E. Rittweger, J. Engelhardt, and S. W. Hell, Angew. Chem.-Int. Edit. **47**, 2685 (2008).

[11] V. A. Vlaskin, N. Janßen, J. van Rijssel, R. Beaulac, and D. R. Gamelin, Nano Lett. **10**, 3670 (2010).

[12] R. Viswanatha, J. M. Pietryga, V. I. Klimov, and S. A. Crooker, Phys. Rev. Lett. **107**, 067402 (2011).

[13] S. B. Piepho and P. N. Schatz, *Group Theory in Spectroscopy with Applications to Magnetic Circular Dichroism* (Wiley, New York, 1983).

[14] J. K. Furdyna and J. Kossut (eds.), *Diluted Magnetic Semiconductors* (Academic, New York, 1988).

[15] B. T. Jonker, Y. D. Park, B. R. Bennett, H. D. Cheong, G. Kioseoglou, and A. Petrou, Phys. Rev. B **62**, 8180 (2000).

[16] D. D. Awschalom (ed.), *Spin Electronics* (Kluwer Academic Publishing, Boston, 2004).

[17] C. Rüster, T. Borzenko, C. Gould, G. Schmidt, L. W. Molenkamp, X. Liu, T. J. Wojtowicz, J. K. Furdyna, Z. G. Yu, and M. E. Flatté, Phys. Rev. Lett. **91**, 216602 (2003).

[18] W. H. Brumage, C. R. Yarger, and C. C. Lin, Phys. Rev. **133**, A765 (1964).

[19] S. T. Ochsenbein, Y. Feng, K. M. Whitaker, E. Badaeva, W. K. Liu, X. Li, and D. R. Gamelin, Nat. Nanotechnol. **4**, 681 (2009).

[20] D. S. McClure, J. Chem. Phys. **39**, 2850 (1963).

[21] U. W. Pohl and H.-E. Gumlich, J. Cryst. Growth **101**, 521 (1990).

[22] U. W. Pohl and H.-E. Gumlich, Phys. Rev. B **40**, 1194 (1989).

[23] C. Benecke, W. Busse, H.-E. Gumlich, and U. W. Pohl, Phys. Status Solidi B **128**, 701 (1985).

[24] H.-E. Gumlich, J. Lumin. **23**, 73 (1981).

[25] W. Busse, H.-E. Gumlich, B. Meissner, and D. Theis, J. Lumin. **12**, 693 (1976).

[26] D. Langer and S. Ibuki, Phys. Rev. **138**, A809 (1965).

[27] T. Dietl, P. Peyla, W. Grieshaber, and Y. Merle d'Aubigne, Phys. Rev. Lett. **74**, 474 (1995).

[28] J. Kreissl, Phys. Status Solidi A **97**, 191 (1986).

[29] J. Kreissl and W. Gehlhoff, Phys. Status Solidi A **81**, 701 (1984).

[30] J. K. Nandagawe, P. K. Patil, P. R. Bote, and R. D. Lawangar-Pawar, Solid State Commun. **77**, 513 (1991).

[31] R. S. Title, Phys. Rev. **131**, 2503 (1963).

[32] G. Abraham, H. Nelkowski, H. Pradella, J. Sahm, and K. Zink, Phys. Status Solidi B **132**, K133 (1985).

[33] R. Roehrig, Ph.D. thesis, University of Freiburg, 1973.

[34] J. Ferguson, H. J. Guggenheim, and Y. Tanabe, J. Appl. Phys. **36**, 1046 (1965).

[35] O. S. Wenger, R. Valiente, and H. U. Güdel, Phys. Rev. B **64**, 235116 (2001).

[36] O. Goede, W. Heimbrodt, and D. D. Thong, Phys. Status Solidi B **126**, K159 (1984).

[37] H. U. Güdel, Comments Inorg. Chem. **3**, 189 (1984).

[38] P. I. Archer, S. A. Santangelo, and D. R. Gamelin, J. Am. Chem. Soc. **129**, 9808 (2007).

[39] E. J. McLaurin, V. A. Vlaskin, and D. R. Gamelin, J. Am. Chem. Soc. **133**, 14978 (2011).

[40] P. Reiss, M. Protière, and L. Li, Small **5**, 154 (2009).

[41] See Supplemental Material at http://link.aps.org/supplemental/10.1103/PhysRevB.89.115312 for additional experimental and computational details, spectroscopic data, and computational results.

[42] R. W. G. Wyckoff, *Crystal Structures* (Interscience Publishers, New York, 1963).

[43] E. Badaeva, Y. Feng, D. R. Gamelin, and X. Li, New J. Phys. **10**, 055013 (2008).

[44] L.-W. Wang and J. Li, Phys. Rev. B **69**, 153302 (2004).

[45] X. Huang, E. Lindgren, and J. R. Chelikowsky, Phys. Rev. B **71**, 165328 (2005).

[46] M. J. Frisch, G. W. Trucks, H. B. Schlegel, G. E. Scuseria, M. A. Robb, J. R. Cheeseman, G. Scalmani, V. Barone, B. Mennucci, G. A. Petersson, H. Nakatsuji, M. Caricato, X. Li, H. P. Hratchian, A. F. Izmaylov, J. Bloino, G. Zheng, J. L. Sonnenberg, M. Hada, M. Ehara *et al.*, Gaussian, Inc., Wallingford, CT, 2011.

[47] J. P. Perdew, K. Burke, and M. Ernzerhof, Phys. Rev. Lett. **77**, 3865 (1996).

[48] J. P. Perdew, K. Burke, and M. Ernzerhof, Phys. Rev. Lett. **78**, 1396 (1997).

[49] C. Adamo and V. Barone, J. Chem. Phys. **110**, 6158 (1999).

[50] W. R. Wadt and P. J. Hay, J. Chem. Phys. **82**, 284 (1985).

[51] P. J. Hay and W. R. Wadt, J. Chem. Phys. **82**, 270 (1985).

[52] E. Badaeva, J. W. May, J. Ma, D. R. Gamelin, and X. Li, J. Phys. Chem. C **115**, 20986 (2011).

[53] E. Badaeva, C. Isborn, Y. Feng, S. Ochsenbein, D. Gamelin, and X. Li, J. Phys. Chem. C **113**, 8710 (2009).

[54] B. Peng, W. Liang, M. A. White, D. R. Gamelin, and X. Li, J. Phys. Chem. C **116**, 11223 (2012).

[55] R. Beaulac, Y. Feng, J. W. May, E. Badaeva, D. R. Gamelin, and X. Li, Phys. Rev. B **84**, 195324 (2011).

[56] D. Fournier, A. C. Boccara, and J. C. Rivoal, J. Phys. C: Solid State Phys. **10**, 113 (1977).

[57] R. E. Behringer, J. Chem. Phys. **29**, 537 (1958).

[58] We note that the saturation magnetization of P_{TI} appears to depend on Mn^{2+} concentration, progressing to larger apparent S values at higher Mn^{2+} concentrations (approaches $S = 4$ at 3.5%; see Supplemental Material [Ref. 41]). This behavior is tentatively attributed to the effects of higher nuclearity Mn^{2+} clusters in the higher concentration samples, but this trend has not been investigated in detail. For this reason, the analysis in Fig. 4 focuses on a low-concentration sample where only monomers and dimers are prominent.

[59] R. Beaulac and D. R. Gamelin, Phys. Rev. B **82**, 224401 (2010).

[60] B. E. Larson, K. C. Hass, H. Ehrenreich, and A. E. Carlsson, Phys. Rev. B **37**, 4137 (1988).

[61] J. Blinowski, P. Kacman, and J. A. Majewski, Phys. Rev. B **53**, 9524 (1996).

[62] H. Weihe and H. U. Güdel, J. Am. Chem. Soc. **120**, 2870 (1998).

[63] H. Weihe and H. U. Güdel, Inorg. Chem. **36**, 3632 (1997).

[64] H. Weihe, H. U. Güdel, and H. Toftlund, Inorg. Chem. **39**, 1351 (2000).

[65] I. B. Bersuker and V. Z. Polinger, *Vibronic Interactions in Molecules and Crystals* (Springer-Verlag, Berlin, Heidelberg, 1989).

[66] L. R. Bradshaw, J. L. Dempsey, V. Z. Polinger, R. Beaulac, A. M. Schimpf, E. J. McLaurin, V. A. Vlaskin, S. A. Crooker, and D. R. Gamelin (unpublished).

[67] A. M. Jawaid, S. Chattopadhyay, D. J. Wink, L. E. Page, and P. T. Snee, ACS Nano **7**, 3190 (2013).